Progress In Electromagnetics Research M, Vol. 138, 22–32, 2026

(Received 18 March 2026, Accepted 13 April 2026, Scheduled 3 May 2026)

A Compact Shared-Aperture MIMO Antenna System for Microwave and Millimeter-Wave V2X Communications

Xiao-Mei Ni[1], Xin-Hao Ding[2, *], Zhen Tan[2], Xin Wang[2], and Ming-Zhu Du[2]

[1]*School of Aeronautic Engineering, Nanjing University of Industry Technology, Nanjing 210023, China*
[2]*School of Information Science and Technology, Nantong University, Nantong 226019, China*

ABSTRACT: To meet the stringent space constraints and diverse connectivity requirements of modern intelligent connected vehicles, a compact MIMO antenna system designed for microwave and millimeter-wave (mm-wave) vehicle-to-everything (V2X) communications is presented. The proposed antenna features a compact footprint adaptable for integration into space-limited automotive modules, such as shark fin antenna housings. By employing a structure reuse technique, the system integrates a four-element microwave MIMO array and two orthogonal mm-wave phased arrays within a size of 30 mm × 30 mm × 2 mm. In the microwave band, a parasitic patch is introduced to achieve dual-mode resonance, ensuring a wide bandwidth for reliable control signaling. Two orthogonal rows of metallized cavities serve a dual purpose: acting as decoupling structures for the microwave MIMO system and functioning as mm-wave arrays to enable two-dimensional beam scanning. This capability is crucial for overcoming blockage effects in dynamic vehicular environments. Experimental results demonstrate that the proposed antenna achieves wide coverage in the microwave band (4.62–5.11 GHz) and high-gain beam scanning (±40°) in the mm-wave band (25.8–30.4 GHz). The measured isolation exceeds 17 dB with an envelope correlation coefficient below 0.11, validating its suitability for next-generation vehicle terminals.

1. INTRODUCTION

With the rapid evolution of Intelligent Transportation Systems (ITS), Vehicle-to-Everything (V2X) communication has become a cornerstone for autonomous driving and road safety [1, 2]. Modern vehicle terminals are required to support multi-band connectivity, utilizing the sub-6 GHz microwave band for reliable control signaling and the millimeter-wave (mm-wave) band for high-data-rate sensor data transmission [3]. However, the vehicular communication environment is complex, often suffering from severe signal blockage caused by large vehicles [1]. Consequently, antenna systems with robust Multiple-Input Multiple-Output (MIMO) capabilities and flexible beam scanning are indispensable.

A critical challenge in designing these systems is the stringent constraint on installation space. For aesthetic and aerodynamic reasons, vehicle antennas are typically enclosed in compact housings, such as the standard "shark fin" module on the roof. As conceptually illustrated in Figure 1, accommodating both broad-beam microwave elements and directional mm-wave arrays within such a confined volume is highly challenging but essential for establishing reliable V2X links. Therefore, developing compact, high-performance shared-aperture antennas suitable for such integration has become a research focus [4, 5].

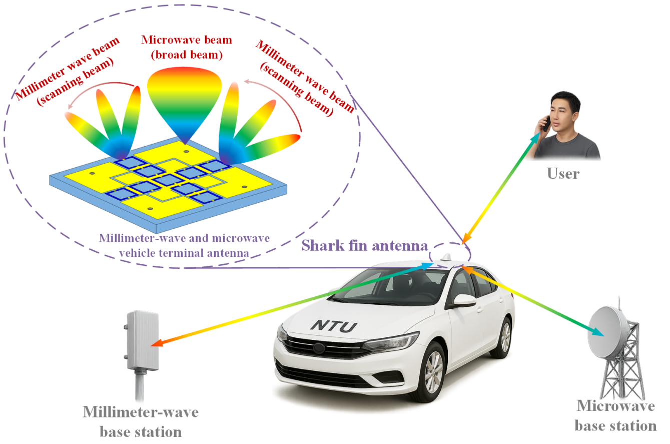

FIGURE 1. Conceptual illustration of the proposed compact shared-aperture MIMO antenna system suitable for integration into an automotive shark fin module. The schematic depicts the broad-beam radiation in the microwave band for robust coverage and wide-angle beam scanning in the millimeter-wave band for directional V2X communications.

To improve aperture efficiency and space utilization, shared-aperture technology has been extensively investigated. To date, there are a lot of studies on shared-aperture antennas using various techniques. In order to realize shared-aperture antennas, microwave and mm-wave antennas can be placed next to each other [6] or placed one above the other [7, 8]. While simple to implement, adjacent placement leads to a large footprint, and stacked placement often results in a higher profile. Such bulky designs are often unsuitable for the streamlined integration required by modern vehicular electronics.

Embedded structures usually present a more compact size [9–13]. Several recent reports using embedded structures have realized the integrated design of microwave antennas

---

* Corresponding author: Xin-Hao Ding (xhding1@hotmail.com).

doi:10.2528/PIERM26031804

Published by THE ELECTROMAGNETIC ACADEMY

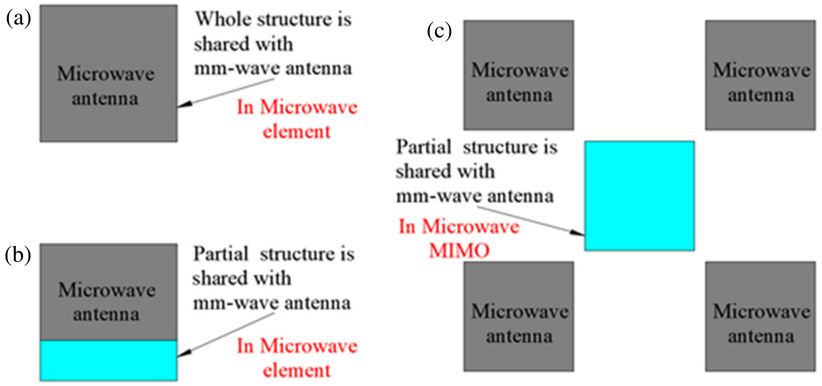

FIGURE 2. Antenna design concept. (a) The whole microwave structure is shared with a mm-wave antenna in a microwave elementary antenna. (b) Part of the microwave structure is shared with a mm-wave antenna in a microwave elementary antenna. (c) Partial structure is shared with the mm-wave antenna in a microwave MIMO antenna system.

and a mm-wave phased array supporting beam scanning [11–13], which is of great significance to match the dynamic connectivity requirements of moving vehicles.

The structure reuse technique presents a significant advantage of high aperture utilization. In [14], mm-wave parabolic reflectors are realized by using periodic metal gratings, and microwave as well as mm-wave parabolic antennas share the same radiating aperture. In these designs, almost 100% of the radiating structure of the microwave antenna is reused by the mm-wave antenna, as illustrated in Figure 2(a). The microwave reflector is implemented by a full metal wall, while the mm-wave reflector is made of a metal grating-based bandgap structure. However, the high degree of mutual containment makes it difficult to add multiple feed ports, limiting the realization of mm-wave beam scanning.

Alternatively, a partial structure of the microwave antenna has been reused as an mm-wave antenna [15–23], as schematically illustrated in Figure 2(b). For instance, a partial structure of a radiating slot in a microwave annular slot antenna has been reused as an mm-wave connected slot phased array [15]. Tapered slots in Vivaldi antennas have also been exploited to function as an mm-wave phased array [16].

However, microwave MIMO antenna system has not been extensively investigated in vehicular environments. In [11, 12, 22], MIMO functionality is implemented but at the expense of a significantly larger planar footprint. Achieving microwave MIMO within compact dimensions remains a significant challenge, especially when considering the limited volume of automotive shark fin modules [4, 5]. Furthermore, ensuring high gain and wide-angle scanning to overcome blockage [1] while maintaining compact size [24–26] is critical. Despite the existing efforts, most reported designs suffer from one or more of the following limitations: limited beam scanning range, insufficient isolation between multiple functions, or lack of integration between orthogonal radiation modes. These gaps motivate the proposed design.

To address the outlined challenges, this work introduces a compact MIMO antenna system designed for microwave and mm-wave vehicle terminal applications employing a structure reuse technique. The proposed design is compact enough to be potentially integrated into standard automotive housings (e.g., shark fin modules). The detailed design concept is schematically presented in Figure 2(c). Compared to existing antennas, this design exhibits the following advantages:

1) Two orthogonal rows of metallized cavities functioning as two mm-wave arrays are introduced into the microwave MIMO system as a decoupling structure for the first time. The metallized cavities can interface with up to four microwave elements, achieving satisfactory isolation between the microwave elements within a compact size.

2) In addition to the reuse of the structure between microwave and mm-wave antennas, the design incorporates the sharing of a parasitic patch among microwave elements to enhance the bandwidth of microwave antennas while maintaining a compact size.

3) Two orthogonal rows of mm-wave arrays realize wide-angle beam scanning with two polarizations.

4) The design is only composed of one antenna substrate and one feed substrate, resulting in a simple structural design and low-cost structure.

2. ANTENNA CONFIGURATION

The antenna system configuration depicted in Figure 3 features a MIMO system, including four microwave patches and two orthogonal rows of mm-wave arrays formed by metallized cavities. This design incorporates an antenna substrate (Sub1) and a feed substrate (Sub2). Sub1 is made from FR4, which has a dielectric constant $\varepsilon_{r1} = 4.4$ and a loss tangent $\tan\delta = 0.02$, while Sub2 is made from RO4003C material with dielectric constant $\varepsilon_{r2} = 3.55$ and $\tan\delta = 0.0027$. The antenna then consists of four microwave patches, a parasitic patch, and two orthogonal rows of metallized cavities. The four microwave patches and the parasitic patch are printed on the upper face of Sub1 while metallized cavities are designed in Sub1. Several slots are etched into the parasitic patch to shift the parasitic patch mode and improve the microwave frequency bandwidth. The metallized cavities serve a dual purpose, acting as a decoupling structure in the microwave frequency band and two antenna arrays in the mm-wave frequency band. Besides, a metal

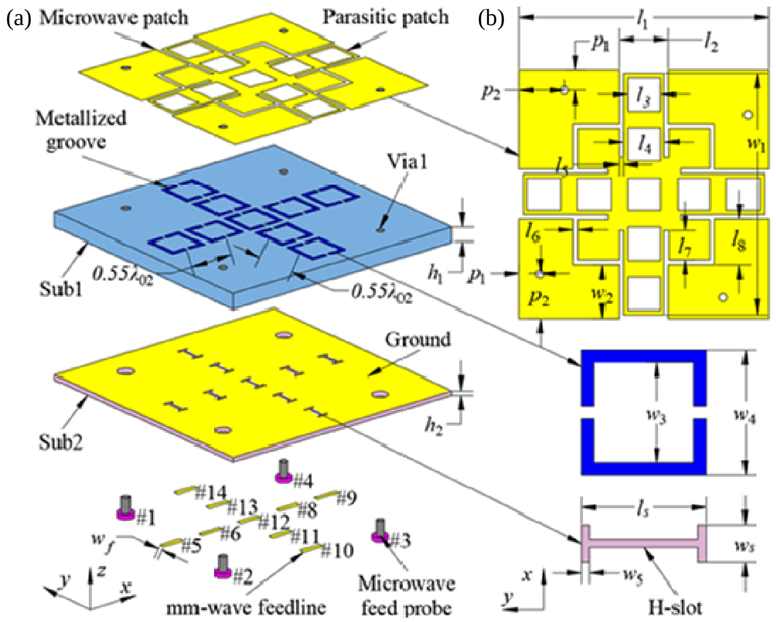

FIGURE 3. Configuration of the proposed dual-band MIMO antenna. (a) 3-D view. (b) Structure of radiating patches, metallized groove, and H-slot.

ground plane (Ground) is printed on the upper face of Sub2. The spacing between the mm-wave elements is $0.5\lambda_{02}$ (λ_{02} is the free-space wavelength at 28 GHz). Each microwave and mm-wave element can be fed independently, where Ports 1, 2, 3, and 4 correspond to the microwave ports, and Ports 5, 6, 7, 8, 9, 10, 11, 12, 13, and 14 correspond to the mm-wave ports. For mm-wave antenna, the feeding mechanism is situated in Sub2, utilizing microstrip lines as feeds for the H-slots etched in the ground plane, which in turn excite the metallized cavities above. In the microwave frequency band, power propagates through the metallic via (Via1) in Sub1 to feed the microwave patch. The geometrical parameters are shown in Table 1.

TABLE 1. Geometrical details of the MIMO antenna (unit: mm).

l_1	l_2	l_3	l_4	l_5	l_6	l_7	L_8	p_1	p_2
30	6	4	5	0.5	0.3	38	5.5	2.5	5.4
l_s	w_1	w_2	w_3	w_4	w_5	w_s	w_f	h_1	h_2
3	29	6	4	5	0.2	0.9	0.7	2	0.305

3. ANTENNA DESIGN

3.1. MIMO System for Microwave Band

Figure 4 shows the evolutionary design process of the four-element MIMO antenna, while the corresponding performance of each model (Case 1, Case 2, Case 3, and Case 4) is shown in Figure 5. The initial MIMO antenna in Figure 4(a) consists of only four patches, and each patch operates in only one mode. It can be observed that the feed position deviates from the diagonal, in order to avoid the reverse current for efficiency improvement [27]. However, the impedance bandwidth is relatively narrow, covering only 4.2% within the frequency range of 4.7 to 4.9 GHz, as illustrated in Figure 5(a). To enhance the bandwidth, the parasitic patch is introduced and placed in the center of the four patches, as shown in Figure 4(b). By implementing this approach, four patches can share the parasitic patch, thereby introducing a new operational mode. However, in Figure 5(b), it can be observed that the isolation between elements is deteriorated, from the original 16 dB to 11 dB, which is obviously unacceptable. Then, to improve isolation, two orthogonal rows of metallized cavities are introduced, as shown in Figure 4(c). As can be seen from Figure 5(c), isolation is improved to above 18 dB. To further reduce the frequency of the parasitic patch mode without increasing the size, several I-slots are judiciously etched into the parasitic patch to extend the current paths, as shown in Figure 4(d). As depicted in Figure 5(d), the introduction of these I-slots results in a shift of the parasitic patch mode frequency from 5.5 GHz to 5.1 GHz, thereby facilitating its merging with the patch mode and achieving dual-mode operation, represented by a reflection coefficient lower than -10 dB. The final design achieves an enhanced impedance bandwidth of 10.7%, encompassing the frequency range spanning from 4.62 GHz to 5.14 GHz, while maintaining a comparable compact size of $0.48\lambda_{01} \times 0.48\lambda_{01}$ (λ_{01} is the free-space wavelength at 4.85 GHz).

To explore the two operating modes, Figures 6(a) and 6(b) show the simulated current distribution at the two distinct resonant frequencies. At 4.7 GHz, a significant current is observed on the microwave patch, suggesting that the lower resonance primarily arises from the microwave patch mode. Conversely, at 5 GHz, the current on the microwave patch is minimal, but a strong current is present on the parasitic patch. This observation indicates that the higher resonance is largely due to the parasitic patch mode. The equivalent electrical circuit model of a single element of the proposed antenna structure is depicted in Figure 6(c). The equivalent circuit in Figure 6 provides a simplified representation of the coupling and resonance behavior. The cavity structure can be modeled as a parallel resonant tank, while the slot introduces capacitive coupling between the

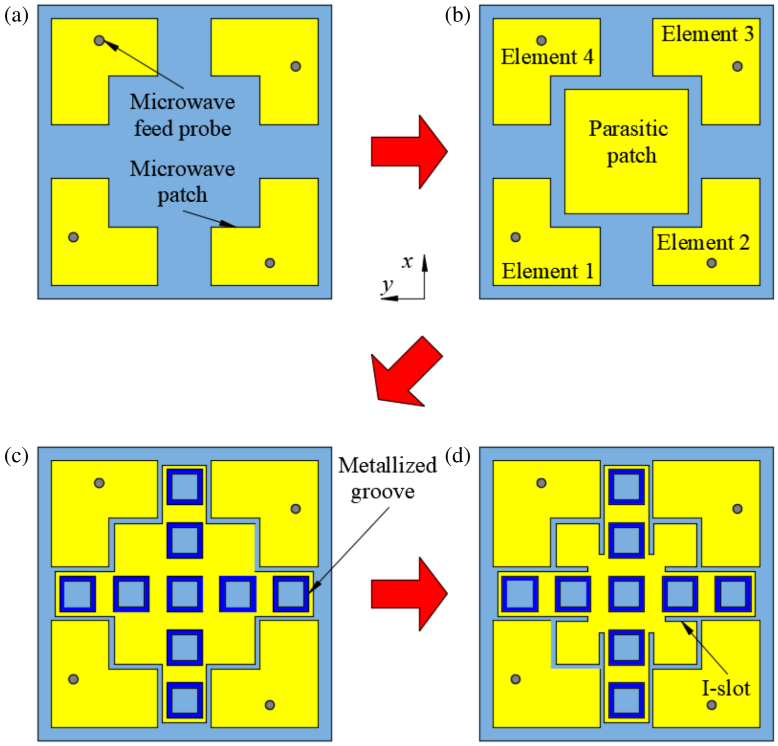

FIGURE 4. Evolutionary design process of microwave MIMO antenna. (a) Case 1, (b) Case 2, (c) Case 3, and (d) Case 4.

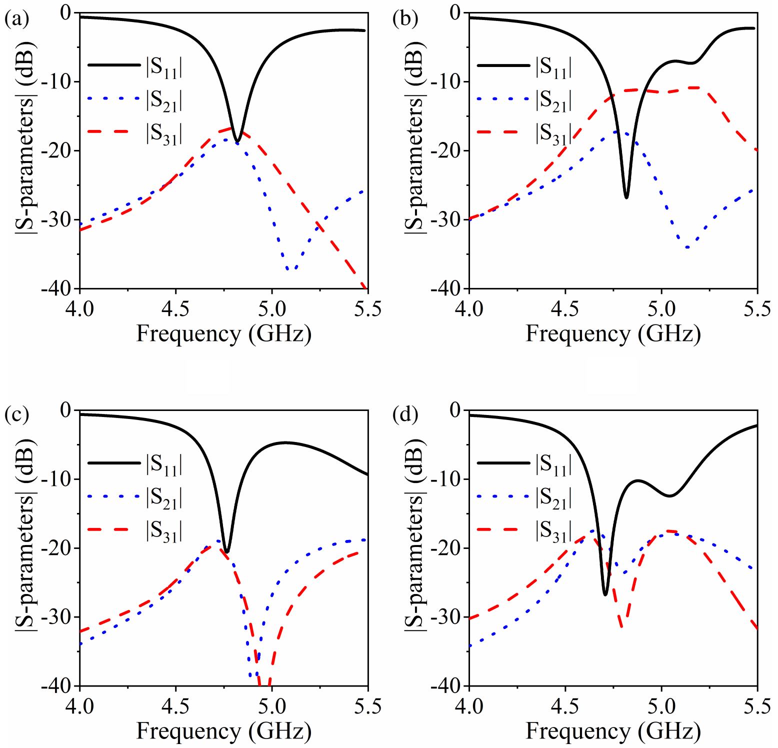

FIGURE 5. Simulated S-parameters of (a) Case 1, (b) Case 2, (c) Case 3, and (d) Case 4 antennas.

feeding structure and the radiator. This model helps explain the impedance matching and the suppression of mutual coupling observed in the design. The elementary microwave radiating patch element and parasitic patch are electrically equivalent to parallel *RLC* resonators. Moreover, while the metallized cavities in the parasitic patch are equivalent to an inductor, the gap between the microwave patch and the parasitic patch is equivalent to a capacitor.

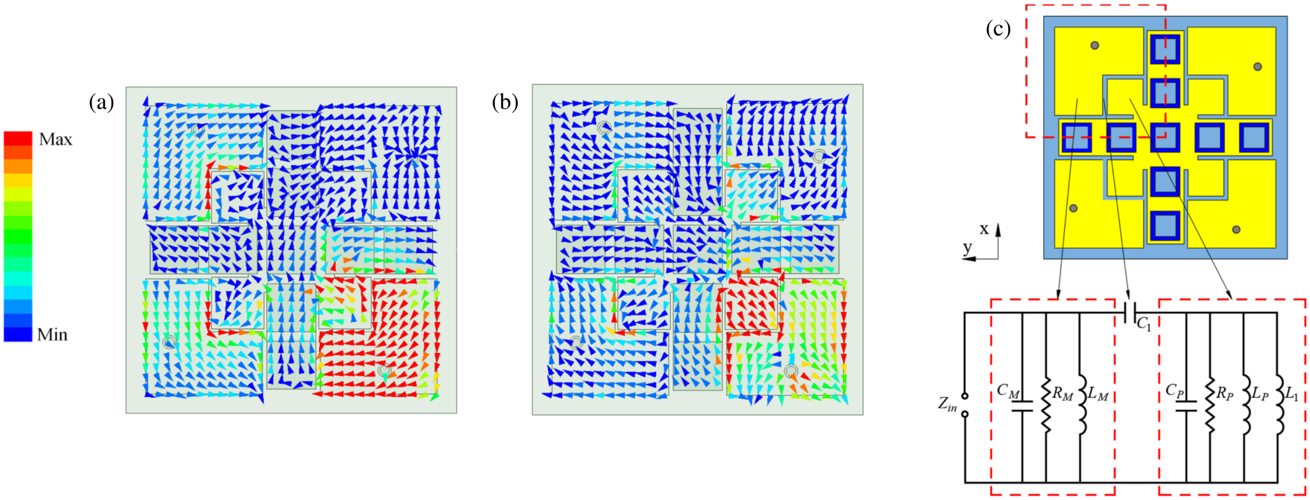

FIGURE 6. (a) Simulated current distribution on the microwave patches and the parasitic patch when Port 2 is excited at 4.7 GHz, and (b) at 5 GHz. (c) Equivalent electrical circuit model of an elementary radiating element of the proposed antenna.

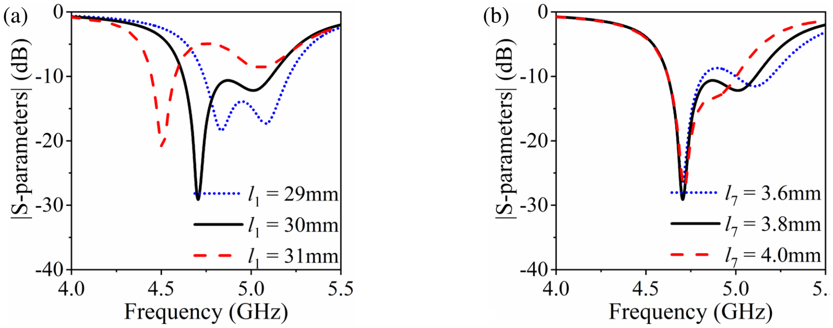

FIGURE 7. Influence of (a) the length of the microwave patch l_1, and (b) the length l_7 of the parasitic patch on $|S_{11}|$.

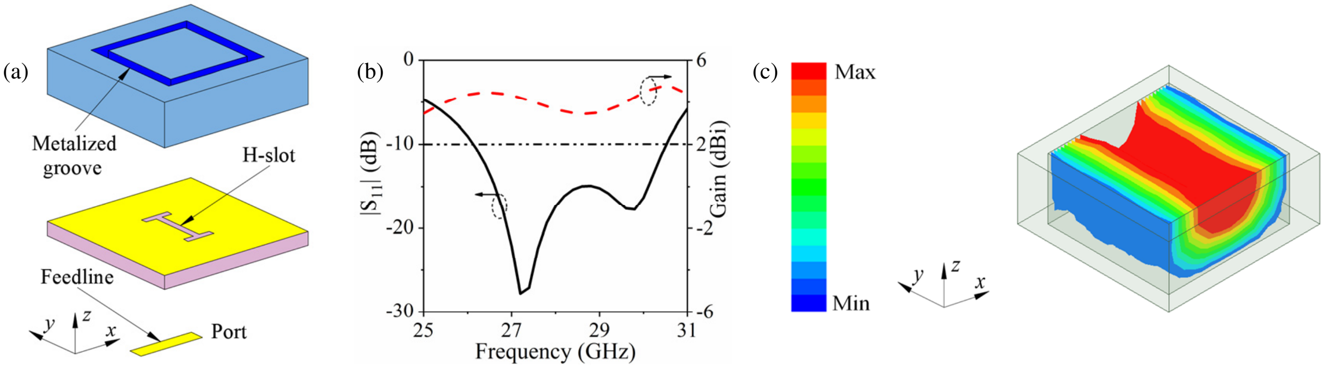

FIGURE 8. (a) Geometry of the mm-wave antenna element. (b) Simulated $|S_{11}|$ and gain of the mm-wave antenna element. (c) Simulated E-field distribution inside the cavity ($TE_{10,1/2}$ mode at 27.5 GHz).

A parametric study is conducted to analyze the design parameters. Figure 7(a) depicts how the length of the microwave patch (l_1) affects $|S_{11}|$. As l_1 increases, the lower mode shifts downward, while the higher mode remains nearly unchanged, indicating that the lower mode is predominantly influenced by the microwave patch. Figure 7(b) shows the impact of the size of the parasitic patch (l_7) on the two modes. Notably, as l_7 increases, the lower mode remains relatively constant, whereas the higher mode shifts downward significantly. This suggests that the higher mode is the parasitic patch mode.

3.2. Antenna for mm-Wave Frequency Band

Based on the metallized cavities acting as the decoupling structure for microwave MIMO antennas, the mm-wave cavity antenna element is designed. As illustrated in Figure 8(a), the dielectric-loaded cavity is constructed using a metallized groove that is grounded. In this design, the cavity antenna functions as a waveguide, exhibiting excellent isolation property, which provides significant design flexibility for the antenna element. The feeding of the element is achieved through an H-shaped slot that is excited by a microstrip line. The antenna

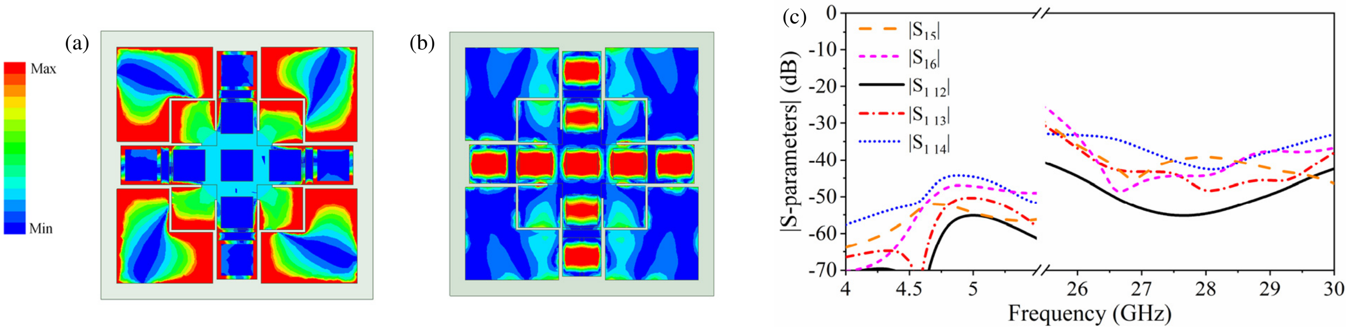

FIGURE 9. Simulated E-field distribution (a) in the microwave frequency band at 4.85 GHz, and (b) in the mm-wave frequency band at 28 GHz. (c) Simulated and measured S-parameters of the antenna prototype in both the microwave and the mm-wave frequency bands.

TABLE 2. Scanning angle and corresponding phase settings.

Scanning angle	x-direction array					y-direction array				
	Port 5	Port 6	Port 12	Port 8	Port 9	Port 10	Port 11	Port 12	Port 13	Port 14
40°	300	150	0	−150	−300	300	150	0	−150	−300
25°	170	85	0	−85	−170	170	85	0	−85	−170
0°	0	0	0	0	0	0	0	0	0	0
−25°	−170	−85	0	85	170	−170	−85	0	85	170
−40°	−300	−150	0	150	300	−300	−150	0	150	300

operates in two modes, including the open-ended waveguide mode (first mode) and the feeding slot mode (second mode). The simulated results indicate a bandwidth of 16.4% (25.9–30.5 GHz) and a peak gain of 4.5 dBi, as shown in Figure 8(b). Furthermore, Figure 8(c) presents the E-field distribution at 27.5 GHz inside the cavity antenna. The electric field rotates around the y-direction, with half a wavelength in the x-direction and a quarter wavelength in the z-direction. It is evident that the distribution aligns with the $\mathrm{TE}_{10,1/2}$ mode characteristics typical of the waveguide structure. The metallized cavities exhibit a frequency-dependent behavior: they operate below the cutoff at microwave frequencies, acting as high-impedance decoupling structures, while supporting propagating waveguide modes at mm-wave frequencies, thus functioning as radiating.

3.3. Analysis of the Integrated Structure

After designing the microwave MIMO antenna and mm-wave element, the dual-band MIMO antenna system for microwave and mm-wave frequencies can be formed. To demonstrate the feasibility of this design concept, the microwave and mm-wave operating frequency bands of the proposed antenna are studied. Figures 9(a) and 9(b) depict simulated E-field distributions at 4.85 GHz and 28 GHz, respectively. At 4.85 GHz, a strong E-field distribution is observed on the microwave patch and parasitic patch, while the E-field on the mm-wave cavity array is very weak. This indicates minimal interference on the mm-wave cavity array when the microwave and parasitic patches are active. Conversely, at 28 GHz, most of the E-field is distributed on the mm-wave cavity array, indicating radiation primarily from the mm-wave cavity array while the microwave antenna remains inactive. Additionally, isolation between different ports is also investigated. As shown in Figure 9(c), the isolation between the microwave and mm-wave ports exceeds 40 dB in the microwave band and exceeds 30 dB in the mm-wave band. The above analysis shows that the proposed antenna can operate independently in the microwave and mm-wave frequency bands with low mutual coupling.

In the mm-wave band, each mm-wave array element can be fed individually. Therefore, beam scanning performance can be achieved by independently adjusting the phase of each element. Moreover, due to the orthogonal arrangement of two sets of metal cavities, beam scanning in two dimensions (*xoz* and *yoz* planes) can be achieved. Achieving a maximum scanning angle often corresponds to meeting criterion of −3 dB scan loss or −5 dB side lobe level (SLL) [13]. According to these criteria, Figure 10 presents the simulated beam scanning performance of the two orthogonal mm-wave arrays. The process of normalized magnitude is as follows: the unnormalized radiation pattern is obtained, the maximum gain in the main beam direction (when the antenna radiates at 0°) is identified. Then, we subtract this maximum gain from all the patterns. In summary, all patterns are normalized with respect to the maximum gain at 0°. It can be observed that both arrays are capable of achieving beam scanning over an angular range of approximately ±40°. The proposed ±40° beam scanning capability provides sufficient spatial coverage to adapt to dynamic blockage and angular variations in vehicular environments, thereby enhancing link robustness in V2X scenarios. The scanning angle and corresponding phase settings are shown in Table 2. The array factor is formulated based on a uniformly spaced linear array model,

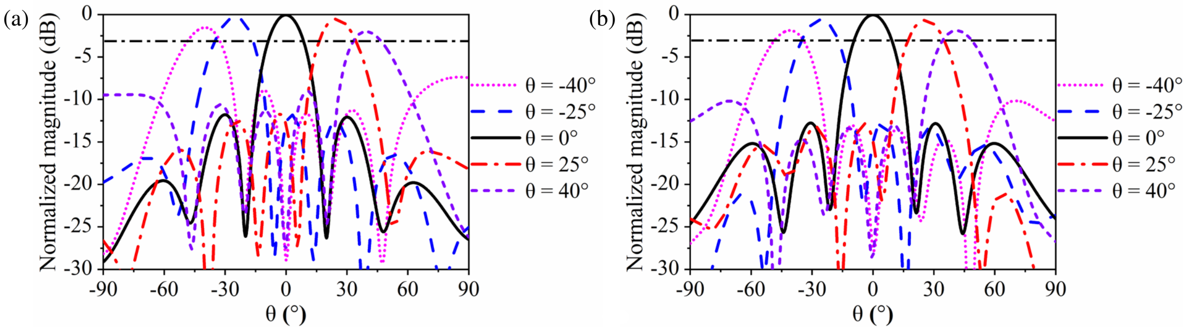

FIGURE 10. Simulated beam scanning of the mm-wave antenna array. (a) E-plane (xoz plane) radiation patterns of the x-direction array. (b) H-plane (yoz plane) radiation patterns of the y-direction array.

where the element spacing is fixed at 0.5λ at 28 GHz. Under uniform amplitude excitation, the overall radiation pattern is determined by the phase progression among elements.

The relationship between the phase increment $\Delta\varphi$ and beam scanning angle θ can be expressed by the array principle: A linear phase gradient steers the main beam away from broadside, where larger phase steps result in larger scanning angles.

4. EXPERIMENTAL VERIFICATION

To experimentally verify the performance of the proposed dual-band MIMO antenna, different prototypes are fabricated using printed circuit board (PCB) technique and tested in an anechoic chamber. The photograph of the prototypes is depicted in Figure 11. Four microwave elements are individually fed with probes (SMA connectors), while six different 1-to-4 Wilkinson power dividers (PD1 to PD6) are designed to test the steered radiation patterns of the two orthogonal mm-wave arrays.

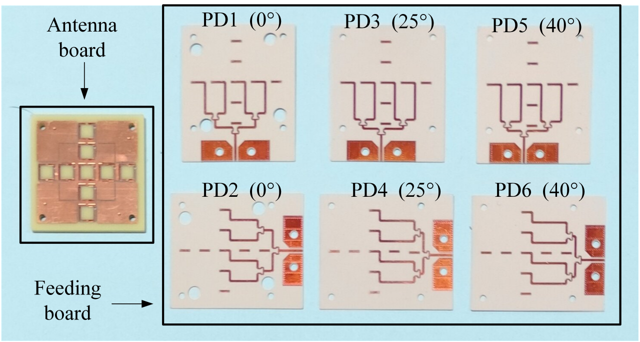

FIGURE 11. Photograph of the fabricated antenna prototypes for different beam scanning. The top feeding boards are for the mm-wave array along x-direction (scanning angles are $0°$, $25°$, and $40°$), and the bottom feeding boards are for the mm-wave array along y-direction (scanning angles are $0°$, $25°$, and $40°$), where PD denotes power divider.

Figure 12(a) presents the reflection coefficients and gain in the microwave band. The -10 dB impedance bandwidth is measured to be 10.1% (from 4.62 GHz to 5.11 GHz), in excellent agreement with the simulated bandwidth of 10.3% (from 4.62 GHz to 5.12 GHz). The gain of the microwave element varies from 1.8 to 2.6 dBi. Figure 12(b) indicates that mutual coupling among the four microwave elements remains below -17 dB within the impedance bandwidth. The simulated and measured total efficiencies in the microwave band show a good agreement, as presented in Figure 12(c). Each antenna element exhibits total efficiencies ranging from 51% to 55% in the microwave operating band. The envelope correlation coefficient (ECC) is crucial for MIMO antennas and is a performance metric that measures the degree of isolation or correlation between communication channels. Here, the discrete method is employed to calculate the ECC, which is given as [28, 29]:

$$\mathrm{ECC}_{ij} = \left| N/\sqrt{D_i D_j} \right|^2$$

$$\text{with } N = \sum_{m,n} E_{\theta,i}^{mn}(E_{\theta,j}^{mn})^* + E_{\phi,i}^{mn}(E_{\phi,j}^{mn})^* w_{mn},$$

$$D_i = \sum_{m,n} |E_{\theta,i}^{mn}|^2 + |E_{\phi,i}^{mn}|^2 w_{mn}, \ \ w_{mn} = \sin\theta_m \Delta\theta\Delta\phi.$$

The smaller the ECC value is, the less the correlation is between antenna elements. The simulated and measured ECCs are shown in Figure 12(d). Measured ECC for the microwave antenna ranges from 0.05 to 0.11, significantly below the threshold of < 0.5 [7], indicating favorable performance. The low ECC is mainly attributed to the combined effect of suppressed mutual coupling provided by the metallized cavities and the pattern diversity introduced by the orthogonal arrangement of the antenna elements. Other important quantities in MIMO systems, such as total active reflection coefficient (TARC), mean effective gain (MEG), and diversity gain (DG) of the MIMO antenna, have been calculated. When all four ports have the same phase, TARC can be calculated as [30, 31]:

$$\mathrm{TARC} = \sqrt{\sum\nolimits_{i=1}^{4} \left| \sum\nolimits_{k=1}^{4} S_{ik} \right|^2 /4}.$$

MEG can be derived from the ECC using [32]:

$$\mathrm{MEG}_i \approx \frac{1}{4}\left(1 - \sum_{j=1}^{4} \eta_j (1 - \mathrm{ECC}_{ij})\right).$$

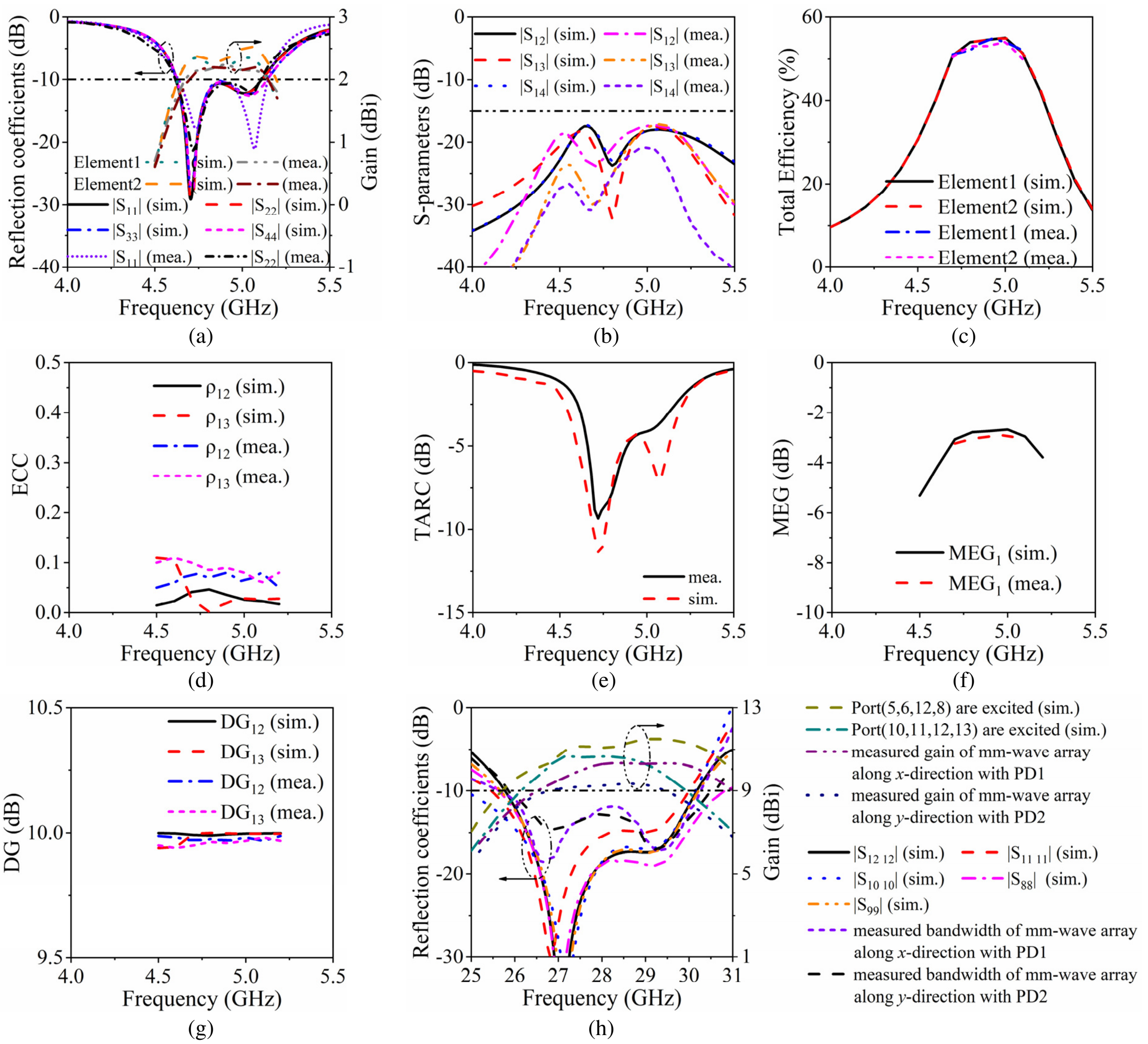

FIGURE 12. Simulated and measured performances of the antenna system. (a) Reflection coefficients and gains. (b) Isolation. (c) Total efficiency. (d) ECC, (e) TARC, (f) MEG, and (g) DG of the microwave MIMO antenna. (h) Reflection coefficients and gains of the two mm-wave antenna arrays.

Finally, DG of the MIMO antenna can be calculated as [33]:

$$\mathrm{DG}_{ij} \approx 10\sqrt{1 - |\mathrm{ECC}_{ij}|^2}\ [\mathrm{dB}].$$

The calculated TARC, MEG, and DG in the microwave band of the MIMO antenna are shown in Figures 12(e), (f), and (g), respectively. The MIMO antenna system features a TARC below -4 dB, and due to the structural symmetry, all the four elements should exhibit the same MEG and DG. The results of Element 1, shown in Figures 12(f)–(g), indicate that the element achieves a MEG lying between -3.5 dB and -2.5 dB. and a DG ranging from 9.8 dB to 10.1 dB.

In Figures 13(a)–(d), simulated and measured radiation patterns are presented at 4.7 GHz and 5 GHz for Element 1 and Element 2 (see Figure 3) in the *xoz* and *yoz* planes and are found to show good agreement. These complementary radiation patterns suggest strong diversity performance, confirming the MIMO system's comprehensive spatial coverage capability.

The simulated and measured reflection coefficients and gains in mm-wave band are presented in Figure 12(h) with good agreement identified. The measured $|S_{11}|$ with PD1 is below -10 dB from 25.6 GHz to 30.3 GHz with a bandwidth of 16.9% while the measured one with PD2 is from 25.8 GHz to 30.4 GHz, corresponding to a bandwidth of 16.4%. The gain of the four-element mm-wave array along x-direction fluctuates in the range of 8.6 to 10.5 dBi while the gain of the four-element mm-wave array along y-direction fluctuates in the range of 8.5 to 9.6 dBi. The radiation patterns of the two mm-wave arrays are also measured. In the same way as for Figure 9, the patterns are normalized with respect to the maximum gain at 0°. The simulated and measured radiation patterns in the E- and H-planes at 28 GHz are plotted in Figures 13(e) and 13(f). It can be observed that the measurements match well with the simulations. mm-wave arrays along the x-axis and y-axis can achieve good beam scanning performance and can achieve a scanning over an angular range of ±40°.

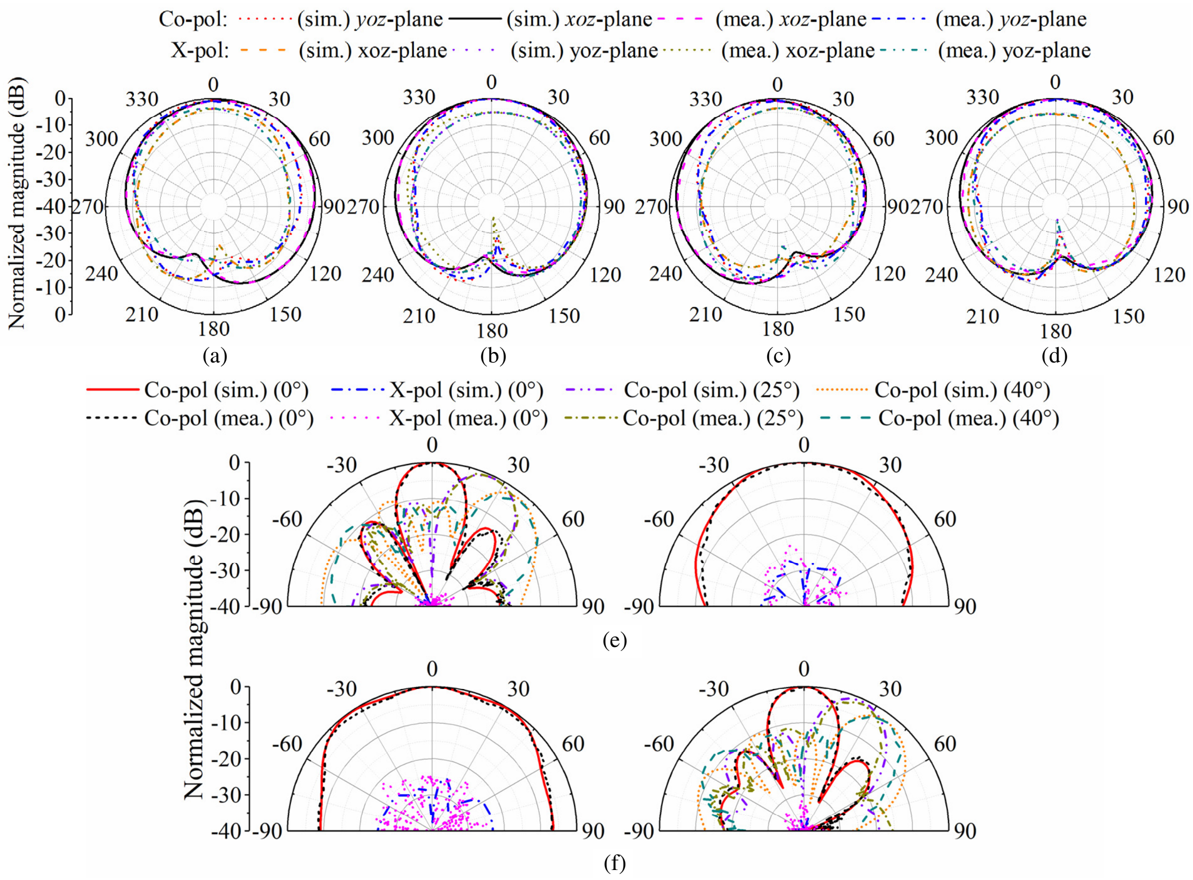

FIGURE 13. Simulated and measured radiation patterns. (a) Microwave Element 1 at 4.7 GHz, and (b) 5 GHz. (c) Microwave Element 2 at 4.7 GHz, and (d) 5 GHz. (e) mm-wave array along x-direction at 28 GHz, and (f) mm-wave array along y-direction at 28 GHz (E-plane on the left and H-plane on the right).

TABLE 3. Performance comparison with the previous antenna designs.

Ref.	f_0 (GHz)	BW (%)	Element electrical dimension (λ_0^3)	Microwave efficiency	Peak gain	MIMO electrical dimension (λ_0^3) (Number of elements)	mm-wave beam-steering ability	MW MIMO	Two-dimensional scanning
[11]	3.5/28	2.9/13.8	-	N.G	7.95/13.94	$0.95 \times 0.43 \times 0.017$ (2)	±45° H-plane	Yes	No
[12]	3.5/28	7.4/12.1	$0.4 \times 0.26 \times 0.04$	N.G	6.6/13.6	$0.4 \times 0.70 \times 0.04$ (2)	±30° H-plane	Yes	No
[13]	3.5/26	11.7/11.9	$0.41 \times 0.3 \times 0.03$	N.G	5/12.9	No	±45° E-plane	No	No
[17]	6.5/28	41.6/6.66	$0.62 \times 0.43 \times 0.14$	74%–86.9%	5.8/8.46	No	No	No	No
[18]	3.5/10.25	40.2/19.5	$\pi \times 0.16^2 \times 0.33$	88%	5.82/12.2	No	No	No	No
[19]	5.915/28	3.7/10.9	$1.27 \times 1.27 \times 0.015$	87%–90%	4.79/11.34	No	No	No	No
[20]	3.5/28	6.3/10.7	$\pi \times 0.7^2 \times 0.012$	N.G	10.65/18.5	No	No	No	No
[22]	3.5/28	13.8/16.1	$0.63 \times 0.32 \times 0.04$	N.G	6.85/13.7	$1.12 \times 0.32 \times 0.04$ (2)	±30° H-plane	Yes	No
[23]	4.7/28	15.8/12.8	$0.42 \times 0.41 \times 0.047$	N.G	5.64/11.33	No	±40° E-plane	No	No
This work	**4.85/28**	**10.1/16.4**	$\mathbf{0.24 \times 0.24 \times 0.03}$	**51%–55%**	**2.6/10.5**	$\mathbf{0.48 \times 0.48 \times 0.03 (4)}$	**±40°∗ E-plane** **±40°∗ H-plane** **±40°# E-plane** **±40°# H-plane**	**No**	**Yes**

λ_0 is the wavelength in the vacuum at microwave center frequency. * This is the simulation result obtained by the five-element mm-wave array. $^\#$ This is the simulation result obtained by the four-element mm-wave array.

Table 3 presents a comparison between the proposed antenna and other antennas reported in the literature. The antennas described in [11, 12, 22] realize microwave MIMO structures. However, they have a significantly larger volume and accommodate only two elements, while our proposed antenna implements microwave MIMO in a very compact size. In [11–13, 22, 23], beam scanning can be achieved, but their space coverage is limited to one dimension. The proposed antenna shows wide-angle beam scanning possibilities in two dimensions. Thus, it is observed that considering the microwave MIMO system with compact size and mm-wave beam scanning capability with high spatial coverage, the proposed antenna demonstrates superior overall performance.

Despite the promising performance, some limitations still exist. The beam scanning range is constrained to ±40°, and the performance degradation at higher frequencies leads to slightly increased side lobe levels. In addition, the fabrication complexity associated with the multilayer structure may pose challenges for large-scale implementation.

5. CONCLUSION

A compact dual-band MIMO antenna system employing a structure reuse technique has been proposed, analyzed, and experimentally verified for microwave and mm-wave vehicle terminal applications. By ingeniously reusing two orthogonal rows of mm-wave cavity arrays as decoupling structures for the microwave elements, the design achieves a highly integrated four-element MIMO system within a compact footprint of 30 mm × 30 mm. This compact form factor makes the antenna highly adaptable for integration into space-constrained automotive modules, such as shark fin housings. The system exhibits broad-beam coverage in the microwave band to ensure reliable control signaling and offers wide-angle 2D beam scanning (±40°) in the mm-wave band to effectively overcome vehicular shadowing effects. Measured results confirm superior performance with isolation exceeding 17 dB and an envelope correlation coefficient below 0.11. These characteristics demonstrate that the proposed shared-aperture antenna is a promising candidate for meeting the diverse and demanding connectivity requirements of future 5G/6G V2X networks.

ACKNOWLEDGEMENT

This work was supported in part by General Project of Basic Science Research in Higher Education Institutions in Jiangsu Province under Grant 23KJB510023, the Youth Program of the Nantong Natural Science Foundation under Grant JC2024046, and the Talent Introduction Project of Nantong University under Grant 135424630060.

REFERENCES

[1] Nguyen, H. T., M. Noor-A-Rahim, Y. L. Guan, and D. Pesch, "Cellular V2X communications in the presence of big vehicle shadowing: Performance analysis and mitigation," *IEEE Transactions on Vehicular Technology*, Vol. 72, No. 3, 3764–3776, Mar. 2023.

[2] Sial, M. N., Y. Deng, J. Ahmed, A. Nallanathan, and M. Dohler, "Stochastic geometry modeling of cellular V2X communication over shared channels," *IEEE Transactions on Vehicular Technology*, Vol. 68, No. 12, 11 873–11 887, Dec. 2019.

[3] Gao, S. and H. Wong, "Triple-band high-gain shared-aperture antenna for internet of vehicles," *IEEE Transactions on Vehicular Technology*, Vol. 74, No. 6, 9380–9390, Jun. 2025.

[4] Xu, J., S. Wen, L. Xu, D. Wang, Z. Wei, and Y. Zhang, "Dual-band shared aperture antenna with wide- and narrow-beam for projectile radio detector," in *2024 14th International Symposium on Antennas, Propagation and EM Theory (ISAPE)*, Hefei, China, 2024.

[5] Wang, W., Z. Zhao, Q. Sun, X. Liao, Z. Fang, K. Y. See, and Y. Zheng, "Compact quad-element vertically-polarized high-isolation wideband MIMO antenna for vehicular base station," *IEEE Transactions on Vehicular Technology*, Vol. 69, No. 9, 10 000–10 008, Sep. 2020.

[6] Wang, D. and C. H. Chan, "Multiband antenna for WiFi and WiGig communications," *IEEE Antennas and Wireless Propagation Letters*, Vol. 15, 309–312, 2016.

[7] Yang, X., L. Ge, Y. Ji, X. Zeng, Y. Li, C. Ding, J. Sun, and K.-M. Luk, "An integrated tri-band antenna system with large frequency ratio for WLAN and WiGig applications," *IEEE Transactions on Industrial Electronics*, Vol. 68, No. 5, 4529–4540, 2021.

[8] Yang, G. and S. Zhang, "Dual-band shared-aperture multiple antenna system with beam steering for 5G applications," *IEEE Transactions on Circuits and Systems II: Express Briefs*, Vol. 69, No. 12, 4804–4808, 2022.

[9] Deng, Q. J., Y. M. Pan, X. Y. Liu, and K. W. Leung, "A singly-fed dual-band aperture-sharing SIW cavity-backed slot antenna with large frequency ratio," *IEEE Transactions on Antennas and Propagation*, Vol. 71, No. 2, 1971–1976, 2023.

[10] Wang, Y. and F. Xu, "Shared aperture 4G LTE and 5G mm-wave antenna in mobile phones with enhanced mm-wave radiation in the display direction," *IEEE Transactions on Antennas and Propagation*, Vol. 71, No. 6, 4772–4782, 2023.

[11] Ma, C. J., Y. M. Pan, X. Y. Meng, and S. Y. Zheng, "A microwave/millimeter-wave shared-aperture antenna based on slow-wave parallel-plate waveguide," *IEEE Transactions on Antennas and Propagation*, Vol. 71, No. 4, 3022–3032, 2023.

[12] Ding, X.-H., W.-W. Yang, H. Tang, L. Guo, and J.-X. Chen, "A dual-band shared-aperture antenna for microwave and millimeter-wave applications in 5G wireless communication," *IEEE Transactions on Antennas and Propagation*, Vol. 70, No. 12, 12 299–12 304, 2022.

[13] Ding, X.-H., W.-W. Yang, W. Qin, and J.-X. Chen, "A broadside shared aperture antenna for (3.5, 26) GHz mobile terminals with steerable beam in millimeter-waveband," *IEEE Transactions on Antennas and Propagation*, Vol. 70, No. 3, 1806–1815, 2022.

[14] Zhu, J., Y. Yang, Z. Hou, S. Liao, and Q. Xue, "Aperture-shared all-metal endfire high-gain parabolic antenna for millimeter-wave multibeam and sub-6-GHz communication applications," *IEEE Transactions on Antennas and Propagation*, Vol. 71, No. 3, 2784–2789, 2023.

[15] Hussain, R., "Shared-aperture slot-based sub-6-GHz and mm-wave IoT antenna for 5G applications," *IEEE Internet of Things Journal*, Vol. 8, No. 13, 10 807–10 814, 2021.

[16] Ren, J., M. Zuo, B. Zhang, X. Du, Z. Chen, Y. Liu, and Y. Z. Yin, "Large frequency ratio Vivaldi antenna system with low-frequency gain enhancement utilizing dual-function taper slot," *IEEE Transactions on Antennas and Propagation*, Vol. 70, No. 6, 4854–4859, 2022.

[17] Sun, Y.-X., K. W. Leung, and K. Lu, "Compact dual microwave/millimeter-wave planar shared-aperture antenna for vehicle-to-vehicle/5G communications," *IEEE Transactions on Vehicular Technology*, Vol. 70, No. 5, 5071–5076, 2021.

[18] Xia, Z.-X., K. W. Leung, P. Gu, and R. Chen, "3-D-printed wideband high-efficiency dual-frequency antenna for vehicular communications," *IEEE Transactions on Vehicular Technology*, Vol. 71, No. 4, 3457–3469, 2022.

[19] Jabeen, S., Q. U. Khan, and S. A. Sheikh, "A single-layer S/C/K/Ka bands shared aperture antenna with novel feed structure for K/Ka bands," *IEEE Transactions on Antennas and Propagation*, Vol. 71, No. 8, 6965–6970, 2023.

[20] Wang, C., W. Cao, W. Ma, C. Li, and J. Jing, "Dual-band structure reused aperture-sharing antenna with low sidelobe and high gain for 5G communication," *IEEE Antennas and Wireless Propagation Letters*, Vol. 23, No. 4, 1386–1390, 2024.

[21] Lin, Y., S. Zheng, and Z. Liang, "Design of a microwave/millimeter-wave shared-aperture antenna by hybridizing series-fed antenna array and leaky wave antenna," *IEEE Transactions on Antennas and Propagation*, Vol. 72, No. 6, 4764–4772, 2024.

[22] Chen, J.-X., J.-Y. Yang, X.-H. Ding, T.-Y. Yan, Y.-L. Li, and W.-W. Yang, "A microwave/millimeter-wave shared-aperture filtering antenna with reused via structure," *IEEE Transactions on Antennas and Propagation*, Vol. 72, No. 9, 7377–7382, 2024.

[23] Yang, W.-W., Q.-H. Zhang, X. Fan, X. Geng, W. Qin, and J.-X. Chen, "A sub-6 GHz/millimeter-wave dual-wideband shared-aperture antenna by reusing the mushroom structure," *IEEE Transactions on Antennas and Propagation*, Vol. 72, No. 10, 8010–8015, 2024.

[24] Wang, W. and Y. Zheng, "Wideband gain enhancement of a dual-polarized MIMO vehicular antenna," *IEEE Transactions on Vehicular Technology*, Vol. 70, No. 8, 7897–7907, Aug. 2021.

[25] Wang, C., W. Cao, W. Ma, Y. Tong, and Y. Zhu, "A sigle-layer dual-band shared-aperture antenna with high gain and sidelobe suppression based on high-order mode for vehicular communications," *IEEE Transactions on Vehicular Technology*, Vol. 73, No. 1, 473–481, Jan. 2024.

[26] Yang, G.-W. and S. Zhang, "A dual-band shared-aperture antenna with wide-angle scanning capability for mobile system applications," *IEEE Transactions on Vehicular Technology*, Vol. 70, No. 5, 4088–4097, May 2021.

[27] Tian, X. and Z. Du, "Wideband shared-radiator four-element MIMO antenna module for 5G mobile terminals," *IEEE Transactions on Antennas and Propagation*, Vol. 71, No. 6, 4799–4811, 2023.

[28] Blanch, S., J. Romeu, and I. Corbella, "Exact representation of antenna system diversity performance from input parameter description," *Electronics Letters*, Vol. 39, No. 9, 705–707, 2003.

[29] Sharawi, M. S., M. Ikram, and A. Sebak, "A two concentric slot loop based connected array MIMO antenna system for 4G/5G terminals," *IEEE Transactions on Antennas and Propagation*, Vol. 65, No. 12, 6679–6686, Dec. 2017.

[30] Manteghi, M. and Y. Rahmat-Samii, "Broadband characterization of the total active reflection coefficient of multiport antennas," in *IEEE Antennas and Propagation Society International Symposium. Digest. Held in conjunction with: USNC/CNC/URSI North American Radio Sci. Meeting (Cat. No.03CH37450)*, Vol. 3, 20–23, Columbus, OH, USA, 2003.

[31] Sharawi, M. S., *Printed MIMO Antenna Engineering*, Artech House, 2014.

[32] Khalid, M., S. I. Naqvi, N. Hussain, M. Rahman, Fawad, S. S. Mirjavadi, M. J. Khan, and Y. Amin, "4-Port MIMO antenna with defected ground structure for 5G millimeter wave applications," *Electronics*, Vol. 9, No. 1, 71, 2020.

[33] Tran-Huy, D., N. Tran-Viet-Duc, H. Tran, and N. Hussain, "A compact MIMO antenna with high gain and dual circular polarization using a T divider for WLAN applications," *Scientific Reports*, Vol. 15, No. 1, 22106, 2025.